nature catalysis

ARTICLES

https://doi.org/10.1038/s41929-018-0044-2

Efficient hydrogen peroxide generation using reduced graphene oxide-based oxygen reduction electrocatalysts

Hyo Won Kim[1,2], Michael B. Ross[3], Nikolay Kornienko[3], Liang Zhang[4], Jinghua Guo[4,5], Peidong Yang[3,6,7] and Bryan D. McCloskey[1,2]*

Electrochemical oxygen reduction has garnered attention as an emerging alternative to the traditional anthraquinone oxidation process to enable the distributed production of hydrogen peroxide. Here, we demonstrate a selective and efficient non-precious electrocatalyst, prepared through an easily scalable mild thermal reduction of graphene oxide, to form hydrogen peroxide from oxygen. During oxygen reduction, certain variants of the mildly reduced graphene oxide electrocatalyst exhibit highly selective and stable peroxide formation activity at low overpotentials (<10 mV) under basic conditions, exceeding the performance of current state-of-the-art alkaline catalysts. Spectroscopic structural characterization and in situ Raman spectroelectrochemistry provide strong evidence that sp^2-hybridized carbon near-ring ether defects along sheet edges are the most active sites for peroxide production, providing new insight into the electrocatalytic design of carbon-based materials for effective peroxide production.

Hydrogen peroxide (H_2O_2) is a valuable chemical with rapidly growing demand in a variety of industries, including the paper and pulp, textile, and electronic industries, wastewater treatment, chemical oxidation (including the large-scale production of propene oxide from propene oxidation) and others[1]. The global H_2O_2 market demand was 3,850 kilotonnes in 2015 and is expected to reach roughly 6,000 kilotonnes in 2024, corresponding to US$6.4 billion (www.gminsights.com/pressrelease/hydrogen-peroxide-market). H_2O_2 is currently generated at an industrial scale through the well-established anthraquinone oxidation process[1]. However, this process is a multi-step method involving expensive palladium hydrogenation catalysts that generate substantial organic byproduct waste[1]. Furthermore, the transport, storage and handling of bulk H_2O_2 are hazardous and therefore expensive, making the distributed on-demand production of H_2O_2 highly desirable[1]. Thus, electrochemical routes to H_2O_2 production through the oxygen reduction reaction (ORR) have attracted attention because of the advantages afforded by such processes, including low energy utilization and cost-effectiveness[1–5]. We focus on H_2O_2 synthesis in alkaline environments, where the reaction bath may be directly used in certain applications, such as bleaching and the treatment of acidic waste streams[6]. However, for electrochemical ORR to achieve these advantages, selective, efficient and cost-effective electrocatalysts need to be developed.

In general, electrochemical ORRs can proceed through one of two reactions in an alkaline electrolyte: the $4e^-$ process to convert O_2 to H_2O (equation (1)) or the $2e^-$ process to form HO_2^- (equation (2))[7].

$$O_2 + 2H_2O + 4e^- \rightarrow 4OH^- \qquad U^o = 1.23\ \text{V versus RHE} \qquad (1)$$

$$O_2 + H_2O + 2e^- \rightarrow HO_2^- + OH^- \qquad U^o = 0.76\ \text{V versus RHE} \qquad (2)$$

U^o is the standard equilibrium potential for each reaction, calculated from the free energy of each reaction[7,8], and RHE is the reversible hydrogen electrode. The reaction shown in equation (1) is important for alkaline fuel cell cathodes, where the energy from fuel oxidation is harnessed electrochemically[1,9,10], whereas the reaction shown in equation (2) forms the environmentally friendly oxidant HO_2^- (H_2O_2 in acidic media or its deprotonated anion but HO_2^- in alkaline media; we will use H_2O_2 and HO_2^- interchangeably throughout this article)[2–6]. Of course, both reactions are extremely useful, especially if they can occur exclusively. The focus of this study is the efficient and selective catalysis of the reaction in equation (2). Electrode compositions that efficiently and selectively catalyse either reaction are desired with an overpotential as close to zero as possible. Numerous materials have been explored as potential electrocatalysts for the production of H_2O_2 from O_2 reduction, including precious metals, transition metals, metal oxides, bimetallic alloys and carbon materials[3,4,11–23]. Of note, the state-of-the-art electrocatalysts for the reaction in equation (2) in acidic conditions are palladium–mercury alloys[3,4].

As a result, an important goal is to develop a practical, cost-effective H_2O_2 formation electrocatalyst that exhibits high activity, selectivity and stability. To this end, we report a robust, metal-free catalyst formed through an easily scalable mild reduction of graphene oxide (mrGO), and present a simple method for preparing a few-layered mrGO electrode (*F*-mrGO) that disallows catalyst aggregation. We annealled the *F*-mrGO electrodes at 600 °C (*F*-mrGO(600)) and found further improvement of the mrGO electrocatalytic oxygen reduction performance. Both the *F*-mrGO and *F*-mrGO(600) catalysts exhibited highly selective and stable HO_2^- formation activity with virtually no applied overpotential in alkaline electrolytes under

[1]Department of Chemical and Biomolecular Engineering, University of California, Berkeley, CA, USA. [2]Energy Storage and Distributed Resources Division, Lawrence Berkeley National Laboratory, Berkeley, CA, USA. [3]Department of Chemistry, University of California, Berkeley, CA, USA. [4]Advanced Light Source, Lawrence Berkeley National Laboratory, Berkeley, CA, USA. [5]Department of Chemistry and Biochemistry, University of California, Santa Cruz, CA, USA. [6]Chemical Science Division, Lawrence Berkeley National Laboratory, Berkeley, CA, USA. [7]Materials Sciences Division, Lawrence Berkeley National Laboratory, Berkeley, CA, USA. *e-mail: bmcclosk@berkeley.edu

© 2018 Macmillan Publishers Limited, part of Springer Nature. All rights reserved.

pure O_2 or ambient air conditions. Ex situ materials characterization in combination with in situ Raman spectroelectrochemistry were performed on both materials and indicated that defects related to ether groups, such as epoxides, along the basal plane or at the sheet edges are active sites for HO_2^- production, thereby providing insights into potential optimization for these and related carbon-based catalysts.

Results

Electrocatalytic peroxide production using mrGO catalysts. Initially, we focused on the synthesis of mrGO and the preparation of *F*-mrGO electrodes. Unlike graphene oxide (GO), typical reduced graphene oxide (rGO) easily aggregates in solution due to strong hydrophobic interactions between the rGO sheets[24]. However, our mrGO synthesis procedure was optimized to prevent this aggregation (see Methods for a detailed procedure). This method resulted in slight reduction (oxygen loss) of the GO (Supplementary Fig. 1) and produced an aqueous solution of well-dispersed single or few-layered mrGO (Supplementary Fig. 2). rGO aggregation is also a typically overlooked issue when preparing electrodes to characterize rGO, as rGO can aggregate during the drying process, thereby substantially reducing the accessibility of the rGO basal planes to reactants[24]. We therefore optimized electrode preparation to disrupt mrGO aggregation, allowing active sites along the mrGO basal plane to remain accessible. We used AvCarb P50 carbon paper—a porous conductive carbon—as a substrate for our electrochemical measurements given its poor ORR activity above 0.6 V versus RHE (Supplementary Fig. 3), ease of processing and cost. After trials consisting of various deposition techniques, we found that simply dip-coating P50 sheets into the well-dispersed mrGO solution, followed by quickly removing water from the coated substrate and drying at ~100 °C, provided an optimal, non-aggregated mrGO coating. The mrGO loading weight was about 10 μg cm^{-2}, which is similar to the mass loading typically used in electrocatalyst characterization studies (Supplementary Table 1). We envision that this method could be easily modified to enable a simple traditional roll-to-roll process (Supplementary Fig. 4).

As confirmation of the few-layered mrGO coating, Raman spectroscopy on dip-coated electrodes exhibited a relatively sharp and single 2D Raman peak shift at 1,680 cm^{-1} (Supplementary Fig. 5), as has previously been observed for few-layered (under 5) rGO assemblies[25]. In contrast, using a more conventional drop-casting method for mrGO electrode preparation, where an excess of the well-dispersed mrGO solution was dropped onto a P50 substrate and subsequently dried, no 2D Raman shifts were observed (Supplementary Figs. 5 and 6)[24], indicating mrGO aggregation (*A*-mrGO) on the electrode surface (Supplementary Fig. 7). Oxygen reduction measurements using linear sweep voltammetry (LSV) in well-mixed oxygen-saturated alkaline electrolytes confirmed that the *F*-mrGO electrode had a higher specific activity at a given applied voltage, as well as a higher onset potential, than the *A*-mrGO sample (Fig. 1a), although both outperformed a standard carbon black-based electrode with high surface area (Vulcan XC72 carbon). These combined results indicate that more active sites are accessible on the *F*-mrGO electrodes compared with the *A*-mrGO electrodes. High activities were also observed when *F*-mrGO was deposited onto a glassy carbon electrode (Supplementary Fig. 8) and characterized using LSV at a rotating disk electrode (RDE; inset of Fig. 1a). In fact, higher activities were observed at the RDE compared with the porous P50 electrodes, presumably due to a reduction in mass transport limitations. Of note, a P50 electrode coated with non-reduced GO exhibited a similar current response to a pristine P50 electrode (Supplementary Fig. 9), indicating that the synthesized GO in this study had no metal impurities (Supplementary Fig. 10) that may have influenced ORR activity. Both the P50 substrate and a GO-coated P50 electrode have little activity above 0.6 V, implying that GO only becomes catalytically active after being slightly reduced.

The estimated equilibrium potential for 2e$^-$ ORR (equation (2)) is 0.825 V versus RHE when taking into account the non-idealities of a 0.1 M KOH solution (see the Supplementary Information for the equilibrium potential calculation). Therefore, at the onset potential for the *F*-mrGO electrode (~0.8 V), ORR can theoretically proceed through either 4e$^-$ or 2e$^-$ ORR (equation (1) or (2), respectively), such that the characterization of selectivity between the two reactions is important. To do so, we used a modified hermetically sealed electrochemical H-cell (Supplementary Fig. 11) that allowed direct quantification of oxygen consumption, as well as a quantitative peroxide titration. The modified H-cell had an easily calibrated headspace volume and an in-line pressure transducer to quantify O_2 pressure decay during ORR (Supplementary Fig. 12). This H-cell therefore afforded direct quantitative oxygen consumption detection during electrochemical measurements, providing accurate determination of ORR selectivity, which we report as Faradaic efficiency: total electrons consumed per oxygen molecule (e^-/O_2). This setup is unique for ORR characterization as it also allows selectivity measurements immediately at the onset potential for ORR. In contrast, typical ORR catalyst selectivity analyses use a RDE or rotating ring disk electrode (RRDE), which relies on achieving mass transport limitations at modest to high overpotentials. Furthermore, when characterizing selectivity using RDE or RRDE, the hydrodynamic boundary layer can be influenced by the surface roughness inherent in attaching the catalyst to the electrode surface, which can reduce the accuracy of the analytical solution of the coupled momentum and mass balances initially derived by Levich for a smooth electrode surface[26,27]. Our analysis provided accurate measurements of selectivity through the direct quantitative measurement of oxygen consumption, regardless of catalyst surface roughness. For example, we measured a 4.0 e^-/O_2 process during oxygen reduction at a commercial platinum/carbon catalyst in an alkaline electrolyte (Supplementary Fig. 13).

The cumulative e^- and O_2 consumptions during chronoamperometry (constant potential: 780–820 torr O_2) measurements are shown at a variety of applied voltages over time scales (Fig. 1b and Supplementary Fig. 14) that allow excellent accuracy for Faradaic efficiency calculations. Two important conclusions were gleaned from these results. First, regardless of the applied potential, a 2.0 e^-/O_2 process was observed (the average of all measurements in Fig. 1b is 2.00 ± 0.03 e^-/O_2). This observation was supported by monitoring O_2 consumption during LSV, where a ~2 e^-/O_2 process was observed at potentials as low as 0.1 V (Supplementary Fig. 15). Second, a 2 e^-/O_2 process was observed for potentials as high as 0.80 V. In a well-poised cell (0.01 M HO_2^-; 0.1 M KOH and 800 torr O_2), where the equilibrium potential of the peroxide formation reaction (equation (2)) could be precisely calculated (0.796 V at these concentrations and pressures), we observed HO_2^- formation activity onset at 0.78 V (Supplementary Fig. 16), corresponding to a remarkably small overpotential of 16 mV. Although we did not attempt ORR measurements at overpotentials less than 10 mV, the actual onset potential for 2e$^-$ ORR on *F*-mrGO is probably in this range. An iodometric H_2O_2 titration (see Methods for a description of the titration procedure) was also performed on the electrolyte after the chronoamperometry measurements to confirm HO_2^- formation consistent with oxygen consumption measurements (that is, a 1.0 O_2/H_2O_2 process was observed; see inset of Fig. 1b). Of note, we observed the selective 2e$^-$ process regardless of the catalyst loading weight, and no additional peroxide reduction properties at modest (>0.4 V versus RHE) potentials (Supplementary Fig. 17). This indicates that our mrGO materials did not catalyse a 2 + 2 electron transfer mechanism, as has been observed on some electrocatalysts, such as those based on Fe–N–C motifs, where loading-dependent selectivities were observed[28].

© 2018 Macmillan Publishers Limited, part of Springer Nature. All rights reserved.

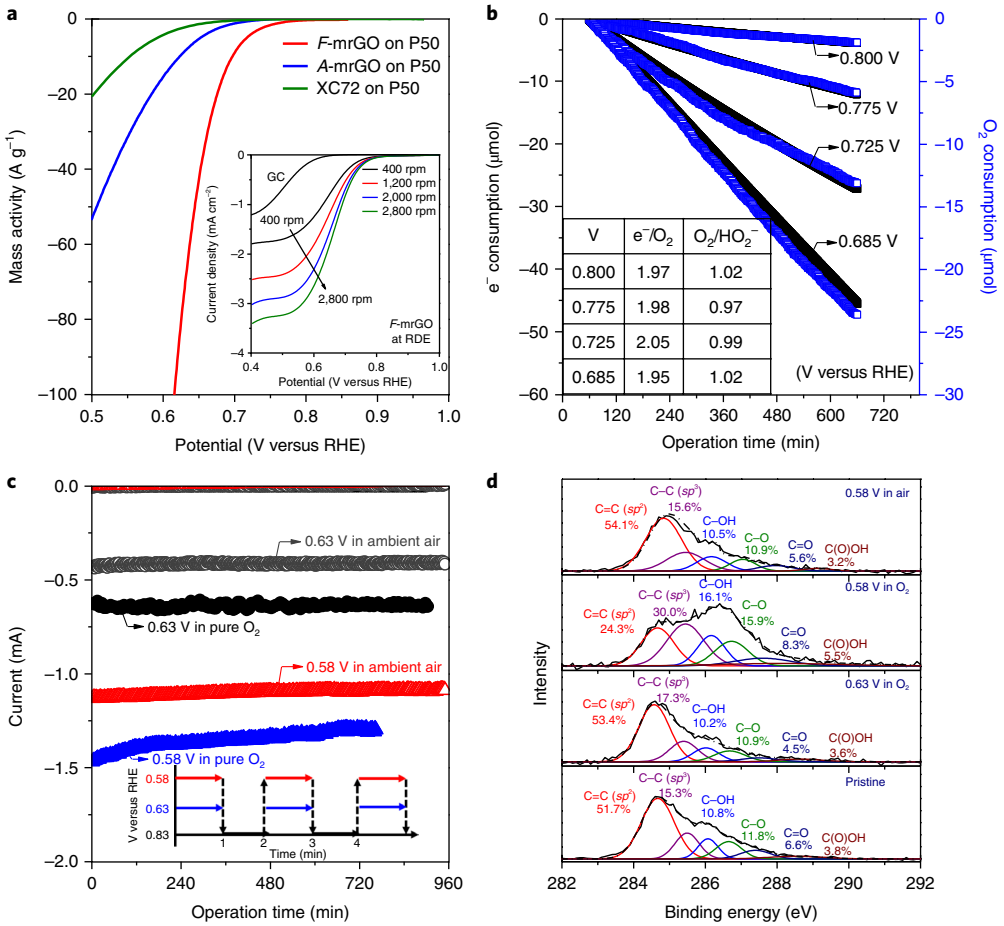

Fig. 1 | *F*-mrGO electrocatalytic properties for the ORR. a, Electrochemical O_2 reduction behaviour of the as-prepared *F*-mrGO, *A*-mrGO and XC72-based electrodes (P50 porous carbon paper as a catalyst support) measured by cathodic LSV (2.0 mV s^{-1}) in an H-cell (~800 torr O_2 saturated 0.1 M KOH solution). Inset is the cathodic LSV (10.0 mV s^{-1}) at a glassy carbon (GC) rotating disk coated with mrGO (rotation rates noted in rpm). An uncoated GC electrode LSV (2,800 rpm) is shown for comparison. Typical mrGO powder loading is 10 μg cm^{-2} for *F*-mrGO in both RDE and porous electrode configurations, 200 μg cm^{-2} for *A*-mrGO and 200 μg cm^{-2} for XC72. **b**, Chronoamperometry in the same electrolyte at an *F*-mrGO electrode at various potentials. The inset table is the corresponding e^-/O_2 from in situ pressure decay measurements and O_2/HO_2^- where HO_2^- was quantified from iodometric HO_2^- titrations on the electrolyte extracted from the working electrode chamber after each measurement. **c**, Long-term stability of *F*-mrGO in either O_2 saturated (~800 torr O_2) or air-exposed 0.1 M KOH. The potential was cycled using the voltage programme shown in the inset: repeating cycles of 1 min at various potentials—0.63 or 0.58 V, followed by 1 min at 0.83 V, at which no measurable current was observed. The electrode surface area was 0.5 cm^2 (10 μg cm^{-2} mrGO). **d**, Structural changes in *F*-mrGO before and after long-term stability measured at 0.63 and 0.58 V (versus RHE) in either O_2 or air. XPS data were collected on the *F*-mrGO electrodes before and after the long-term stability tests shown in **c**.

The catalyst current response at 0.63 V under pure O_2 also remained constant during the course of a long-term measurement (Fig. 1c; the current plotted was that measured at the end of each 1 min cycle), implying good stability of the catalyst over long operational periods at these modest overpotentials. Although catalyst instability was observed at larger overpotentials in pure O_2 conditions (for example, an applied potential of 0.58 V; Fig. 1c), *F*-mrGO stability improved at lower oxygen partial pressures (for example, in ambient air) at applied potentials down to 0.45 V (0.58 V is shown in Fig. 1c and 0.45 V is shown in Supplementary Fig. 18), allowing larger current rates to be achieved while still maintaining catalyst stability. In support of these electrochemical stability observations, X-ray photoelectron spectroscopy (XPS) characterization of the electrodes indicated no structural changes in the catalyst composition during a 16 h chronoamperometry cycling measurement (using the programme shown in the inset of Fig. 1c) when operated at 0.63 V in pure O_2 or 0.58 V in ambient air (Fig. 1d), although large changes were observed in the electrode operated at 0.58 V in pure O_2 (Fig. 1d and Supplementary Fig. 19). From an iodometric H_2O_2 titration performed on the electrolyte, the total amount of H_2O_2 formed during the measurement that provided an optimal current rate and stability (0.45 V under ambient air for 15 h) corresponds to 37 mg H_2O_2 produced per 10 μg of mrGO. Taken together, these results confirm that *F*-mrGO is an excellent catalyst for HO_2^- formation: it is highly selective, active at overpotentials as low as ~0.01 V and stable at potentials where HO_2^- is formed at high rates.

In situ Raman spectroelectrochemical analysis of *F*-mrGO. In general, the structural heterogeneity of rGO materials makes the identification of catalytically active sites difficult[29–31], and our *F*-mrGO catalysts were no different. XPS indicated that numerous oxygen-containing functional groups, including ether, hydroxyl, ketone and carboxylic acid groups, were present in the mrGO catalyst (Supplementary Fig. 1). In an attempt to identify the active site in our mrGO catalysts for HO_2^- formation, we pursued two approaches: in situ Raman characterization, which we used to probe catalyst–adsorbate interactions during catalysis, and further thermal treatment to modify the mrGO oxygen defect composition.

© 2018 Macmillan Publishers Limited, part of Springer Nature. All rights reserved.

Raman spectroscopy has been used extensively to characterize the structure of carbon-based materials[32]. Thus, we used in situ Raman spectroelectrochemistry to probe any transient adsorbate–catalyst interactions that occurred during oxygen reduction. Such spectroscopic characterization of carbon electrolcatalysts during oxygen reduction is lacking, thereby limiting the understanding of how to improve electrocatalyst activity[15–23]. We employed a cell configuration that allowed Raman spectroscopy to be performed at a biased electrode immersed at a very shallow depth in the cell's electrolyte (Supplementary Fig. 20). The *F*-mrGO electrode was characterized at various applied potentials (using chronoamperometry) in an O_2–saturated electrolyte. Of note, no changes in the Raman spectra were observed at these same potentials in an N_2–saturated electrolyte (Supplementary Fig. 21), and the Raman spectra of the *F*-mrGO electrode at open circuit voltage (OCV) with O_2-saturated electrolyte and of a dry *F*-mrGO electrode were similar (Supplementary Fig. 22). We also observed almost identical Raman spectra between an immersed *F*-mrGO in electrolyte with and without peroxide added (Supplementary Fig. 23), indicating that any spectra differences during voltage bias were due to interactions between the catalyst and adsorbed reaction intermediates and not between the HO_2^- product and the catalyst. In addition, the Raman spectra of the pristine P50 electrodes were nearly identical at OCV and the lowest applied potential we probed (0.63 V; Supplementary Fig. 24), indicating that any changes in the Raman spectra were due exclusively to the mrGO catalysts. All fits reported in this study follow the Voigt deconvolution method[31].

Raman spectra of disordered carbon materials typically exhibit four major Raman bands, which are referred to as the G band (~1,580 cm^{-1}), D band (~1,350 cm^{-1}), D′ band (or sometimes G′ band; ~1,620 cm^{-1}) and 2D band (2,680 cm^{-1}). The 2D band is generally related to interactions between neighbouring graphitic planes, indicating variations in sheet stacking or the total number of graphene layers[32]. Although the oxygen atom surface coverage also slightly influences the 2D band, it is difficult to decouple this effect from interplane interactions in rGO-based materials[32]. We therefore focused on the relative intensities and peak broadening of the D and D′ bands relative to the ubiquitous G band. Numerous studies have shown that each of these bands is related to certain defects in oxidized disordered carbon. Of particular importance, the D′ band has been previously ascribed to sp^2 basal plane carbon oxidation in graphene-based materials[32], whereas the D band appears as a result of carbon disorder (for example, sp^3 disorder in graphene basal planes) and graphene planar edge site defects[30]. Therefore, any changes in these Raman peaks during ORR probably indicate an interaction between the corresponding mrGO carbon sites and intermediates for H_2O_2 formation—probably O_2^{-}* or OOH* (* indicating an adsorbed species)[20,32].

As the applied potential decreased from 0.83 to 0.63 V, noticeable changes in the spectra began to evolve at 0.78 V (Fig. 2a,b), indicating the occurrence of an mrGO–adsorbate interaction consistent with the onset of ORR (Fig. 2b and Supplementary Fig. 16). At low overpotentials (where the applied potential was above 0.68 V), several interesting trends were observed: as the overpotential increased, the characteristic D′ band peak area increased and broadened from 42.5–59.2 cm^{-1} at the full-width at half peak maximum (FWHM). However, both the D and G band FWHM and peak area remained relatively constant (Fig. 2b). Given that the D band remained unchanged in the 0.83–0.68 V region, the low-overpotential active sites on *F*-mrGO appeared to not be associated with edge site defects or sp^3-hybridized carbon (the defects ascribed to the D band by others)[32]. Instead, broadening of the D′ band in this same voltage region implied that basal plane sp^2 carbon sites interacted with adsorbed ORR intermediates at low overpotentials, resulting in a Raman response similar to what is observed when such sp^2 carbon is oxidized. This observation suggests that certain sp^2 basal plane carbon sites were catalytically active for 2e⁻ ORR. These are unusual results because most believe that edge sites are more active than basal plane sites in carbon-based materials[33–35], although through mrGO annealing, we will show later that edge sites can also be highly active for HO_2^- formation. Of note, the Raman spectra at OCV before and after an ORR measurement at 0.63 V were statistically similar (Supplementary Fig. 21), indicating that no irreversible oxidation of these sites was observed (as is consistent with the results shown in Fig. 1c,d). At lower applied potentials (0.63 V), all three peaks (D, D′ and G) broadened and the intensity of the D band substantially increased relative to the G and D′ bands (as observed in the ratio of the peak areas in Fig. 2b), implying that edge site and/or sp^3-hybridized carbon defects also interact with adsorbed intermediates at these lower voltages.

Characterization of thermally annealed *F*-mrGO. Based on these results, we hypothesized that the highly active (low overpotential) *F*-mrGO sites were basal plane sp^2 carbons adjacent to certain oxygen functional groups. This hypothesis was tested by electrochemical and physical characterization of thermally annealed *F*-mrGO electrodes. Thermal annealing of GO has previously been shown to substantially reduce GO's oxygen content and influence its oxygen defect site composition[30,31]. In this study, the *F*-mrGO electrodes (with P50 carbon paper as a catalyst support) were first prepared to ensure the electrodes comprised non-aggregated, few-layered mrGO without any binders. These electrodes were then thermally annealed under an N_2 atmosphere. This procedure disallowed the facile preparation of annealed mrGO RDE electrodes, and hence electrochemistry was only performed on porous electrodes. Thermal treatment temperatures were selected to be 300 and 600 °C, as thermogravimetric analysis-mass spectrometry indicated that substantial CO_2 evolution occurred around these temperatures (Supplementary Fig. 25), indicating the removal of oxygen from the mrGO. Although thermal treatment led to the decomposition of oxygen-containing functional groups, the annealed samples maintained their few-layered structure (Supplementary Fig. 26). Of note, the P50 substrate appeared to be thermally stable up to 650 °C under N_2 (Supplementary Fig. 27), as no weight change was observed during a thermal gravimetric analysis measurement. Furthermore, annealing of the pristine P50 substrate at 300 or 600 °C did not change its catalytic activity (Supplementary Fig. 28).

XPS confirmed that thermal annealing substantially reduced the presence of C–O and C=O bonds in the mrGO, with their atomic percentages dropping from 21.8 and 6.1 for mrGO to 1.4 and 1.4 for mrGO annealed at 300 °C, respectively (Fig. 3a). sp^2 carbon bonding in the mrGO annealed at 300 °C increased to 66% from 32% in unannealed mrGO. These results indicate that thermal treatment at 300 °C results in a significant reduction of carbon defects associated with oxygen functional groups on the mrGO basal planes[31].

Although mrGO annealed at 300 °C and coated on P50 (*F*-mrGO(300)) still catalysed a 2e⁻ ORR process at all applied potentials (Supplementary Fig. 29), *F*-mrGO(300) exhibited a lower onset potential and lower specific activity at a given applied potential than unannealed *F*-mrGO (Fig. 3b). This observation, coupled with the smaller oxygen-atomic composition in *F*-mrGO(300) (Supplementary Fig. 30) compared with unannealed *F*-mrGO (Supplementary Fig. 1), suggests that the reduction of oxygen defects during the 300 °C thermal annealing results in a material with lower catalytic activity. XPS (Fig. 3a) indicated that among the oxygen defects initially present, the C–O and C=O concentration in the mrGO catalysts was substantially reduced during the 300 °C annealing, implying that active sites for H_2O_2 production may be related to one (or both) of these groups.

Surprisingly, *F*-mrGO(600) exhibited a higher onset potential during ORR than unannealed *F*-mrGO (Fig. 3b) while still maintaining a 2e⁻ process at all potentials, including 0.815 V versus

© 2018 Macmillan Publishers Limited, part of Springer Nature. All rights reserved.

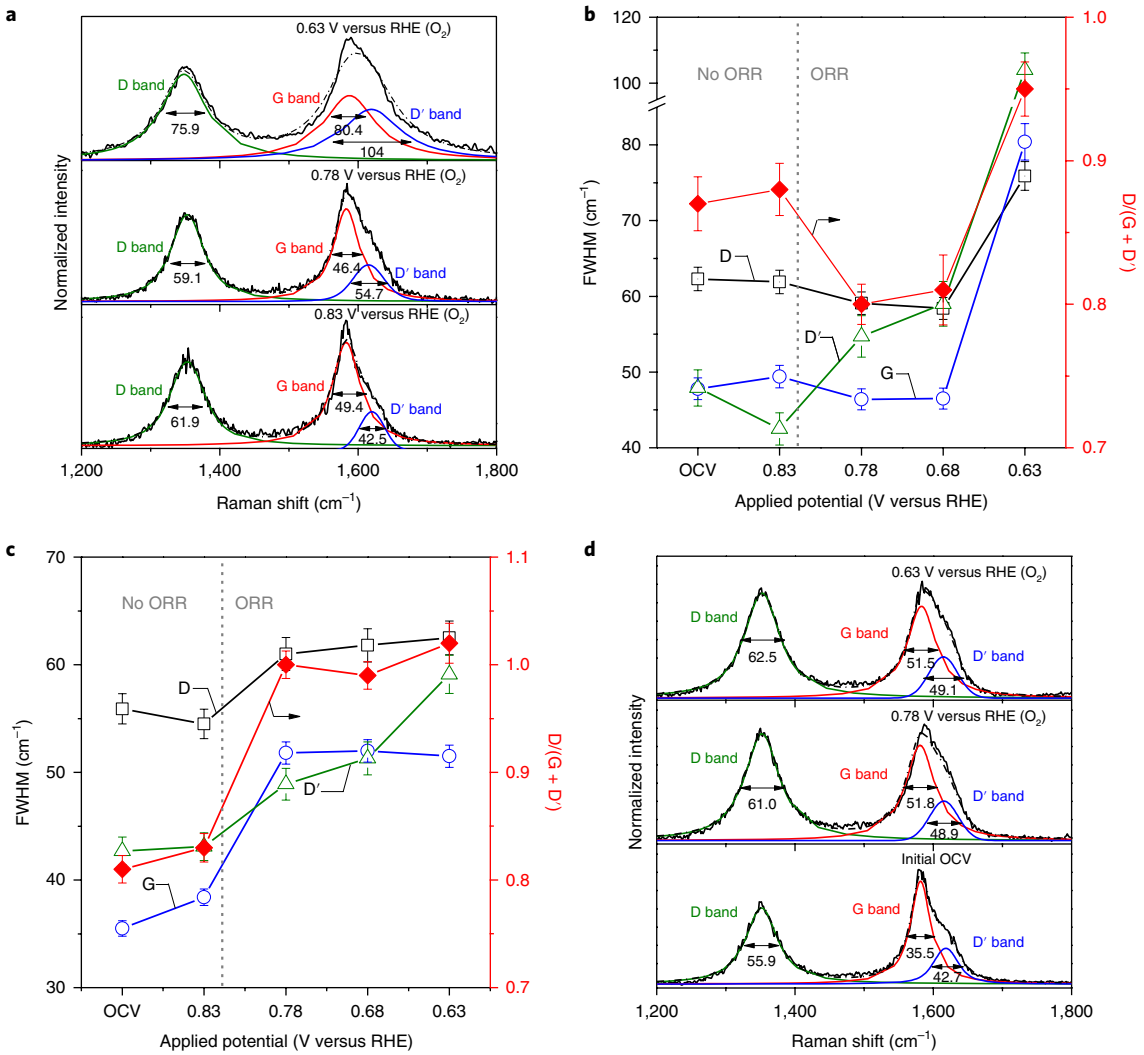

Fig. 2 | Raman spectroelectrochemistry during ORR measurements at *F*-mrGO and *F*-mrGO(600) electrodes. a, In situ Raman spectra—with calculated Voigt deconvolutions—of *F*-mrGO at various potentials. ORR occurs below 0.80 V. **b**, FWHM and D/(G + D′) ratio of *F*-mrGO electrodes as a function of applied potentials. **c**, FWHM and the D/(G + D′) ratio of *F*-mrGO(600) electrodes as a function of applied potentials. In **b** and **c**, the error bars represent the s.d. of three trials. **d**, In situ Raman spectra of *F*-mrGO(600) at various potentials. Oxygen-saturated (~760 torr) 0.1 M KOH was used as the electrolyte.

RHE (Supplementary Fig. 31). In a well-poised cell (0.01 M HO_2^-, 0.1 M KOH and 800 torr O_2), activity was observed at a statistically similar potential to the equilibrium potential (~0.80 V), implying activity with only millivolts of applied overpotential (Supplementary Fig. 32). *F*-mrGO(600) showed high mass activity for H_2O_2 production that exceeded current state-of-the-art electrocatalysts in either acidic or alkaline electrolytes (Fig. 4), although we note that the comparison between electrocatalysts in acidic and alkaline media is not straightforward given the differences in required design criteria between the two systems. The high catalytic activity of *F*-mrGO(600) was unexpected given that the oxygen content in mrGO annealed at 600 °C was much lower than in either mrGO annealed at 300 °C or unannealed mrGO (Supplementary Figs. 1 and 30). However, a combination of structural characterization using XPS, Fourier-transform infrared spectroscopy (FTIR) and near-edge X-ray absorption fine structure (NEXAFS) spectroscopy, as well as in situ Raman spectroscopy, implicated ring ether defect formation along the mrGO sheet edges as the possible origin for this increase in catalytic activity, as is discussed below.

Combined spectroscopic analyses to identify active sites in *F*-mrGO. From XPS characterization of the mrGO materials (Fig. 3a), mrGO annealed at 600 °C showed a dramatic decrease in carboxylic acid group content and a modest increase in ether C–O group content compared with mrGO annealed at 300 °C. This result implies that carboxylic acid groups decompose to generate new ether functional groups, which is consistent with previous reports[30,31]. Carboxylic acid functionalities are known to primarily exist at rGO sheet edges[29], such that we would expect ether groups in *F*-mrGO(600) to be located primarily at sheet edges. In support of this theory, FTIR spectroscopy (Fig. 3c) on powders of annealed and unannealed mrGO showed that a strong and sharp infrared absorption band at 800 cm^{-1} appears in mrGO annealed at 600 °C, which was ascribed in recent reports to ether functionalities at the sheet edges of thermally reduced GO[30,31]. Furthermore, from the O K-edge NEXAFS spectra of dry mrGO powders, sharp and intense peaks at 534.5 and 540.4 eV arose in mrGO annealed at 600 °C (Fig. 3d), even though it had low oxygen content compared with unannealed mrGO and mrGO annealed at 300 °C (Supplementary Figs. 1 and 30). These peaks can be ascribed to transitions of O1s core-level electrons to antibonding π^* states and σ^* states from C–O bonding from ring ether functionalities at the rGO sheet edges[36,37]. These distinct features are explained by locally ordered arrangements of ring ether groups at the sheet edges of the mrGO annealed at 600 °C

© 2018 Macmillan Publishers Limited, part of Springer Nature. All rights reserved.

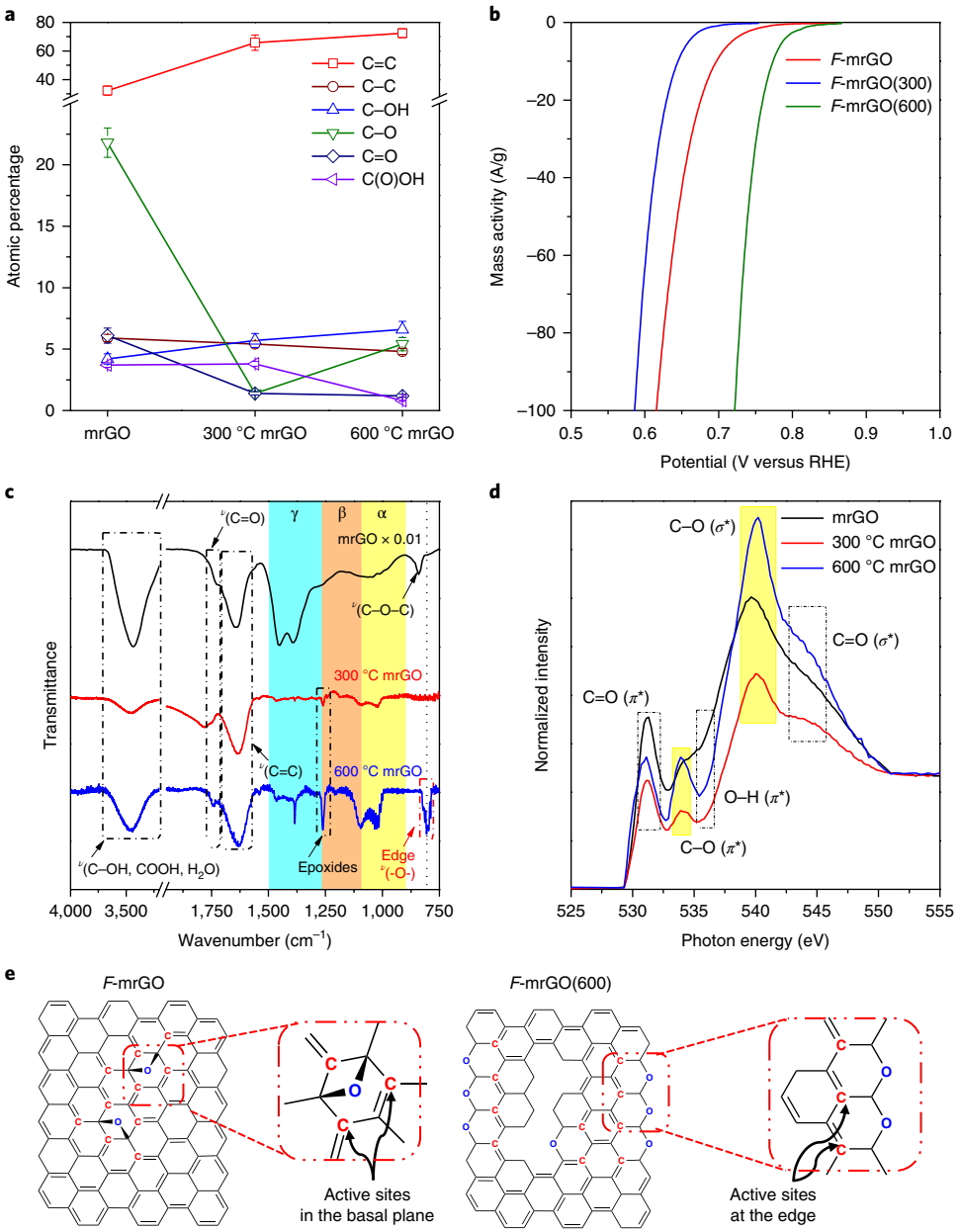

Fig. 3 | Structural characterization and electrocatalytic activity of thermally annealed *F*-mrGO electrodes. a, Atomic ratio of the as-prepared, unannealed mrGO and annealed (300 and 600 °C) mrGO powders measured by C1s XPS. The error bars represent the s.d. of three measurements. **b**, Electrochemical O_2 reduction behaviour of the as-prepared mrGO and annealed mrGOs measured by cathodic LSV (2.0 mV s^{-1}) in O_2-saturated (~800 torr O_2) 0.1 M KOH solution. **c**, FTIR spectra of various mrGO powder samples. Peak assignments are discussed in more detail in the Methods. **d**, High-resolution oxygen K-edge NEXAFS spectra of unannealed and annealed mrGO powder samples. **e**, Idealized schemes of proposed low-overpotential active sites on *F*-mrGO and *F*-mrGO(600).

that result in constructive interference[35]. Combined, our XPS, FTIR and NEXAFS data strongly suggest that mrGO thermal treatment at 600 °C produces ring ether groups at mrGO sheet edges[30,31,36,37]. Furthermore, thermal treatment at 600 °C generates a high concentration of these active ring ether edge sites compared with unannealed mrGO, resulting in higher peroxide formation activity (Fig. 3b). Of note, although the annealing process may influence the electrical conductivity of the mrGO samples, four-point probe measurements on each of the electrodes indicate that the electrical conductivities of *F*-mrGO and *F*-mrGO(600) electrodes are similar to that of the bare P50 substrate and in the range of ~4,000 S m^{-1}. We are therefore confident that conductivity differences probably do not influence our catalytic trends, but further studies would be helpful to rule this possibility out entirely. Furthermore, the long-term activity of *F*-mrGO(600) was equally as stable as unannealed *F*-mrGO under a variety of O_2 partial pressures and applied potentials, including relatively large overpotentials (0.45 V) under either O_2 or ambient conditions (Supplementary Fig. 33).

In situ Raman spectra of the *F*-mrGO(600) electrode during ORR (Fig. 2c,d) also support the suggestion that the active site for HO_2^- formation is related to edge site defects in *F*-mrGO(600). In contrast with the unannealed *F*-mrGO sample, a substantial increase in D band peak intensity was observed once small cathodic overpotentials were applied; that is, D/(G + D′) substantially increased from OCV to 0.78 V (~40 mV overpotential for HO_2^- formation; Fig. 2c). In fact, broadening and increasing peak areas of both the D and

© 2018 Macmillan Publishers Limited, part of Springer Nature. All rights reserved.

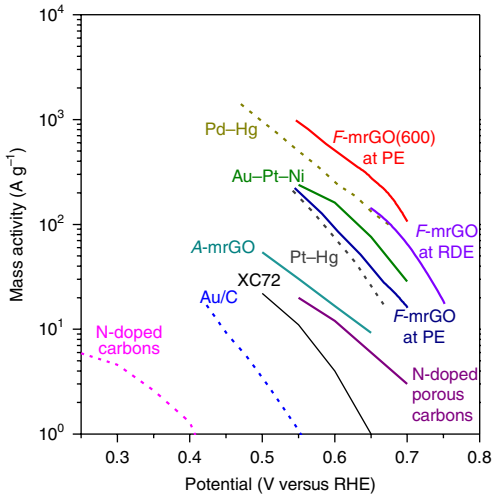

Fig. 4 | Mass activity of different electrocatalysts for H_2O_2 production. Mass activity was calculated using electrochemical data and catalyst loading values from the literature. Further details of these calculations are available in Supplementary Table 1. The data presented as dashed lines were measured in acidic conditions (0.1 M $HClO_4$) and the data presented as solid lines were measured in basic conditions (0.1 M KOH). Data were taken from precious metals and their alloys[3,4,11,13] and carbon-based catalysts[10,14]. Data for XC72, *A*-mrGO, *F*-mrGO at RDE, *F*-mrGO at PE and *F*-mrGO(600) at PE are from the present study, where 'at RDE' and 'at PE' denote values measured in a rotating disk and porous electrode configuration, respectively.

D′ bands were clearly observed at low overpotentials (Fig. 2c,d), indicating that sp^2-hybridized carbon (as has been ascribed to D′ band broadening) located at the sheet edges (as has been ascribed to D band broadening) interacts with adsorbed intermediates in this potential regime. Given the XPS, FTIR and NEXAFS results (Fig. 3), which suggest that ring ether groups are present at sheet edges in *F*-mrGO(600), the Raman results strongly suggest that the active sheet edge sp^2 carbon sites for HO_2^- formation are related to ring ether groups. As for the unannealed mrGO electrode, the Raman spectra at OCV were similar before and after an ORR measurement at lower overpotentials (0.63 V applied potential), confirming the reversibility of this interaction (Supplementary Fig. 34).

Conclusions

In conclusion, carbon-based materials show great promise for electrochemical HO_2^- production from O_2 given their potential affordability and excellent electrocatalytic performance compared to other HO_2^- formation catalysts. Here, we show how to appropriately design a carbon-based electrocatalyst for HO_2^- formation using a suite of capabilities aimed at understanding defect structure and property relationships for rGO catalysts. We suggest that carbon catalysts with high concentrations of epoxy or ring ether groups located either on their basal planes or at plane edges exhibit outstanding electrochemical HO_2^- production in terms of activity (HO_2^- production at <10 mV overpotential), selectivity (~100% 2e$^-$ ORR) and stability (over 15 h at 0.45 V) in alkaline conditions. The best catalyst reported here, *F*-mrGO(600), exhibited activity and selectivity towards HO_2^- production exceeding reported state-of-the-art catalysts. As such, these and related catalysts are very promising candidates for the electrochemical production of HO_2^-. Furthermore, carbon materials are typically used as supports for high-surface-area 4e$^-$ ORR catalysts[8,9], and the knowledge gained here indicates that the design and synthesis of any such materials should involve the elimination of ether-based defects from carbon substrates to improve the 4e$^-$ ORR selectivity.

Methods

Materials. Fine-grade synthetic graphite powder (SP-1) was supplied by Bay Carbon and used as received. Sulphuric acid (H_2SO_4; 97%), hydrochloric acid (HCl; 35% in water) and acetone (CH_3COCH_3; 99.5%) from Daejung Chemicals and Metals, hydrogen peroxide (H_2O_2; 50% in water), phosphorous pentoxide (P_2O_5; 98%) and ethylenediaminetetraacetic acid (ACS reagent) from Aldrich Chemical, and potassium permanganate ($KMnO_4$) from Junsei Chemical were also used as received.

GO synthesis and purification. GO was synthesized using the modified Hummers method. Briefly, sulphuric acid (450 ml) was added to graphite powder (10 g) and the temperature of the solution was maintained below 10 °C and stirred for 90 min. A small amount (1.5 g) of potassium permanganate was added to the mixture and stirred for 90 min. Then, a large amount of potassium permanganate (30 g) was added to the mixture and stirred for 1 h at <10 °C. The solution changed in colour from black to dark green. The solution was then heated to 40 °C and stirred for 1 h. Deionized water (450 ml) was added to the solution in a dropwise fashion and the temperature was maintained below 50 °C to prevent a rapid increase in temperature that could result in a thermal explosion. The solution turned brown. The solution was then heated to 95 °C for 30 min, and hydrogen peroxide solution (10 wt.%; 300 ml) was slowly added to the solution and stirred for 30 min. The solution changed to light yellow. Synthesized GO was purified with hydrochloric acid and acetone. The GO solution was filtered and washed with hydrochloric acid (10 wt%; 5,000 ml) five times. Inductively coupled plasma optical emission spectrometry measurements after each rinse cycle indicated that only after five rinses were no metal impurities present in the GO (Supplementary Fig. 10). Filtered GO cake was dried over phosphorous pentoxide at 40 °C for 24 h under vacuum. The GO powder was redispersed in acetone (5,000 ml) and filtered and washed five times. The cake layer was dried at 40 °C for 24 h under vacuum.

Synthesis of mrGO. The synthesized and purified GO was dispersed homogeneously in water using a sonication bath. The dispersed GO solution (0.1 wt.%) was added to a round-bottom flask (500 ml) and stirred under flowing nitrogen. The prepared solution was maintained at 100 °C and stirred overnight. After completion, the mrGO was filtered and rinsed several times with ultrapure water, and the mrGO was suspended in ultrapure water before use.

Catalyst structural characterization. Raman spectra were recorded using a Horiba Jobin-Yvon LabRAM HR800 μ-Raman instrument. All Raman spectra were acquired with 532 nm excitation from a 250 mW diode laser. The incident laser power was decreased by a factor of 100 to avoid sample damage. For analysis, the D/G ratio and FWHM of D, G and D′ were calculated by deconvoluting the Raman spectra using Gaussian, Lorentz and Voigt (combining Gaussian and Lorentz) peak fitting (Origin 8.5) to allow a comparison of peak areas. All deconvolution methods provided similar results, and the Voigt fitting method is reported throughout this study. Peak fitting and deconvolution followed well-established methods for such analyses[38–40].

Electrical conductivity was measured using a home-built probe station setup. Unannealed and annealed mrGO-coated P50 and pristine P50 (~0.5 cm × 1.0 cm; 0.17 mm thick) were used to measure the electrical conductivity. The sheet resistance of each film was measured using Keithley 2400 source meters in four-wire van-der-Pauw configuration. Ohmic contacts were confirmed before all measurements, and data were acquired using homemade LabVIEW programmes. Electrical conductivity was extracted from the sheet resistance and thickness measurements.

XPS was performed using a monochromatized Al Kα X-ray source (Quantum 2000; Physical Electronics). C1s and O1s peak data were collected to analyse the extent of oxidation of GO, mrGO and annealed mrGO, and all C/O ratios provided were based on the relative peak areas of the C1s and O1s peaks. For detailed analysis, the peaks were deconvoluted into five or six Gaussian peaks to allow a comparison of peak areas after performing a Shirley baseline correction. Deconvolution followed well-established techniques for XPS analysis[41–43].

FTIR spectra of modified GOs were measured using a Bruker model IFS 66 V equipped with a liquid nitrogen cooled mercury cadmium telluride detector (Kolmar model KMPV8-1-J2) with an 8 μm band gap in the range 4,000–1,000 cm^{-1}. Various functional groups were observed, including hydroxyls (broad peak at 3,050–3,800 cm^{-1}), carbonyls (1,750–1,850 cm^{-1}), carboxyls (1,650–1,750 cm^{-1}), C=C (1,500–1,600 cm^{-1}), and ethers and epoxides (1,000–1,280 cm^{-1}), along with an unusual sharp and strong asymmetric ring ether (~800 cm^{-1}) after 600 °C thermal treatment, and regions of spectral overlap involving mostly C–O and C=O contributions (α-region, β-region and γ-region).

NEXAFS experiments were performed on the undulator beamline 8.0.1.4 (wet-resonant inelastic X-ray scattering (RIXS) endstation) at the Advanced Light Source, Lawrence Berkeley National Laboratory. The NEXAFS measurements were recorded in total-electron-yield mode by monitoring the sample drain current. The NEXAFS resolution was set to 0.2 eV for oxygen. The energy scales of the oxygen K-edge NEXAFS spectra were calibrated by the spectrum of a standard TiO_2 sample. The NEXAFS spectra were first divided by the incident beam intensity and then normalized to the absorption pre- and post-edges. The surface morphologies of

© 2018 Macmillan Publishers Limited, part of Springer Nature. All rights reserved.

the prepared electrodes were determined using a field emission scanning electron microscope (JSM-7500F; JEOL). The thermal stabilities of mrGO, P50 and coated P50 were measured by thermal gravimetric analysis coupled with mass spectroscopy (TA Instruments) under an argon atmosphere at a heating rate of 10 °C min^{-1}.

Catalyst-coated porous electrode preparation. The *F*-mrGO electrodes were prepared by immersing a pre-cut strip (2 cm × 0.5 cm) of AvCarb P50 carbon paper (Fuel Cell Store) in a prepared mrGO solution (0.05 wt.%) for 1 min, followed by immediate drying using a heat gun and then drying under ambient conditions at 100 °C overnight. We note that no polymer binders were used in the preparation of the *F*-mrGO electrodes to further avoid unwanted aggregation of mrGO in the casting solution. mrGO adhesion was never problematic during any electrochemical measurements (in particular, constant activity was observed over long-duration measurements).

Thermal annealing of the prepared *F*-mrGO electrodes was performed using a tube furnace at 300 °C (*F*-mrGO(300)) or 600 °C (*F*-mrGO(600)) under N_2. The loading weight of the few-layered mrGO electrodes was measured using a microbalance (XS3DU Microbalance; Mettler Toledo). To more accurately measure the *F*-mrGO electrode loading weight, dip-casting of the large-surface-area P50 (20 cm^2) was performed. Other catalysts, such as *A*-mrGO and XC72, were drop-cast onto P50 using 0.05 wt.% catalyst in water solutions.

The dip-coating procedure is reminiscent of—although certainly more basic than—Langmuir–Blodgett deposition, which has been used to form single-layer GO films on substrates[24]. During the dip-coating procedure, the mrGO physically adsorbed to the immersed P50 carbon substrate, while the individual mrGO sheets were electrostatically repelled from each other due to the presence of oxygen functionalities on their surface. It is likely that the combination of these two effects results in a uniform *F*-mrGO coating while eliminating mrGO aggregation[24]. It is worth noting that no 2D Raman shift was observed when characterizing the mrGO powder (Supplementary Fig. 6), as the powder was also expected to aggregate in its dried state. Comparison of the scanning electrode microscopy images of these electrodes also indicated stark differences in the mrGO morphology on dip-coated and drop-cast electrodes (Supplementary Fig. 7).

RDE preparation. Electrochemical RDE studies were carried out in a conventional three-electrode cell using a Bio-Logic VSP potentiostat. A Pt wire and an Ag/AgCl electrode filled with saturated KCl aqueous solution were used as the counter electrode and reference electrode, respectively. The electrolyte was 0.1 M aqueous KOH solution, which was purged with oxygen for 10 min before the electrochemical test. To prepare the *F*-mrGO-coated glassy carbon electrode, the mrGO was dispersed in water (0.025 wt.% mrGO) by sonication. Some 10.00 µl of this dispersion was transferred onto a glassy carbon electrode (5 mm diameter; 0.196 cm^2 geometric area) embedded in a polytetrafluoroethylene sheath and then dried in air at 80 °C for 30 min. The mrGO loading was calculated to be 10 µg cm^{-2}. LSV was measured using an RDE (MSR analytical rotator; Pine Instrument) at a scan rate of 10 mV s^{-1}.

Electrochemical measurements. Electrochemical measurements were performed using a Bio-Logic SP-300 potentiostat and a custom-built modified electrochemical H-cell (Adams and Chittenden; Supplementary Fig. 11). The voltages of both the counter electrode (Pt wire) and working electrode (catalyst-coated P50; ~1.0 cm^2 exposed to the electrolyte) were recorded simultaneously. An Hg/HgO reference electrode with 1 M NaOH as the electrolyte (Bio-Logic) was used for all measurements. A liquid junction potential of 35 mV, as calculated from the Henderson equation for a continuous-mixture junction[44], was expected from a 0.1 M KOH/1 M NaOH junction and has been included in all reported potentials. All potentials are reported against the RHE and are corrected for ohmic losses. All electrochemical measurements were performed in 0.1 M KOH saturated with pure O_2, typically at ~800 torr unless stated otherwise, or exposed air at ~760 torr. LSV was performed by cathodically sweeping the working electrode potential from open circuit potential (OCV) at a scan rate of 2.0 mV s^{-1}. Chronoamperometry was conducted to accurately identify e^-/O_2 values, as well as onset potentials for ORR.

Quantification of O_2 consumption. The electrochemical H-cell used in this study was custom built to ensure hermetic integrity of both the counter and working electrode chambers, which were separated using a Nafion 117 membrane (Supplementary Fig. 11). The pressure on each side of the cell was analysed individually using an in-line pressure transducer (PX419; Omega Engineering; Supplementary Fig. 12). An Al electrode holder was used to hold the catalyst-coated P50 working electrode. No portion of the Al holder was immersed in the electrolyte. The working electrode chamber electrolyte was stirred vigorously using a magnetic stir bar over the course of the experiment to limit mass transport effects. The volume of each chamber of the H-cell was calibrated using a volume-expansion technique and the ideal gas law. The volumes of the three-port chamber (working electrode and Hg/HgO as a reference electrode) and the two-port chamber (Pt wire as a counter electrode) of the H-cell were 13.4 ± 0.3 ml and 10.6 ± 0.2 ml, respectively. The uncertainty in the volume arises from the Nafion membrane deflecting when the pressure difference between each chamber of the H-cell increased. The three-port and two-port chambers of the H-cell were each filled with 5 ml of electrolyte during each experiment so that the total headspace above the electrolyte in the three-port chamber was calculated to be 8.4 ± 0.3 ml. As O_2 was consumed during ORR at the working electrode, the pressure transducer measured changes in the working electrode chamber pressure. Knowing the pressure decay and calibrated headspace volume, the ideal gas law was used to calculate the total moles of O_2 consumed during ORR.

Hydrogen peroxide quantification. An iodometric titration was conducted to quantify the HO_2^- produced and followed procedures previously used in our laboratory to quantify lithium peroxide formation in Li-air batteries[45] After an ORR measurement, 1.0 ml of the electrolyte, along with 1.0 ml of 2 wt.% potassium iodide solution, 1 ml of 3.5 M sulphuric acid and two or three drops of a molybdate catalyst, was added to a vial. H_2O_2 oxidizes iodide to iodine per the following reaction:

$$H_2O_2 + 2\ KI + H_2SO_4 \rightarrow I_2 + K_2SO_4 + 2\ H_2O \quad (3)$$

The iodine formed was then titrated with a thiosulfate solution of known concentration.

$$I_2 + 2\ Na_2S_2O_3 \rightarrow Na_2S_4O_6 + 2\ NaI \quad (4)$$

Early in the titration, the presence of iodine was easily observed by a characteristic yellow-brown solution colour. In the final stages of the titration (after the solution had reached a pale, yellow colour), starch was added as an indicator to determine the final end point. The end point was achieved when the characteristic blue colour of the starch–iodine complex completely vanished to yield a clear solution.

In situ Raman spectroscopy. In situ Raman measurements were performed using a Jobin-Yvon LabRAM HR confocal microscope with 20× (0.25 NA) objective and a custom-made Teflon electrochemical cell (Supplementary Fig. 20). A 532 nm laser (1–20 mW) was focused on the electrode, and the Raman scattered photons were dispersed by a 1,800 g cm^{-1} grating and collected by a spectrometer. In situ spectroelectrochemistry was performed using a Gamry Interface 1000 potentiostat, a Pt counter electrode (Alfa Aesar; Pt gauze 52 mesh woven from 0.1 mm diameter wire, 99.9% trace metals basis) and a Hg/HgO reference electrode in ~30 ml of 0.1 M KOH. During a measurement, high-purity O_2 or N_2 was bubbled at ~5–10 ml min^{-1}, after which Raman spectra were collected using chronoamperometry at the potential of interest. For analysis, Raman spectra were normalized by laser power and collection time, and corrected by a linear background subtraction. The D/G and D/(D′ + G) ratios were obtained by deconvoluting the Raman spectra using a multi-peak Voigt fit.

Data availability. The data that support the plots within this paper and other findings of this study are available from the corresponding author upon reasonable request.

Received: 24 August 2017; Accepted: 21 February 2018;
Published online: 26 March 2018

References

1. Campos-Martin, J. M., Blanco-Brieva, G. & Fierro, J. L. G. Hydrogen peroxide synthesis: an outlook beyond the anthraquinone process. *Angew. Chem. Int. Ed.* **45**, 6962–6984 (2006).
2. Seh, Z. W. et al. Combining theory and experiment in electrocatalysis: insights into materials design. *Science* **355**, eaad4998 (2017).
3. Siahrostami, S. et al. Enabling direct H_2O_2 production through rational electrocatalyst design. *Nat. Mater.* **12**, 1137–1143 (2013).
4. Verdaguer-Casadevall, A. et al. Trends in the electrochemical synthesis of H_2O_2: enhancing activity and selectivity by electrocatalytic site engineering. *Nano Lett.* **14**, 1603–1608 (2014).
5. Viswanathan, V., Hansen, H. A., Rossmeisl, J. & Norskov, J. K. Unifying the 2e$^-$ and 4e$^-$ reduction of oxygen on metal surfaces. *J. Phys. Chem. Lett.* **3**, 2948–2951 (2012).
6. Chen, Z. et al. Development of a reactor with carbon catalysts for modular-scale, low-cost electrochemical generation of H_2O_2. *React. Chem. Eng.* **2**, 239–245 (2017).
7. Wagman, D. D. et al. The NBS tables of chemical thermodynamic properties. *J. Phys. Chem. Ref. Data* **11**, 2-37–2-355 (1982).
8. Mukerjee, S. & Srinivasan, S. Enhanced electrocatalysis of oxygen reduction on platinum alloys in proton exchange membrane fuel cells. *J. Electroanal. Chem.* **357**, 201–224 (1993).
9. Gasteiger, H. A., Kocha, S. S., Sompalli, B. & Wagner, F. T. Activity benchmarks and requirements for Pt, Pt-alloy, and non-Pt oxygen reduction catalysts for PEMFCs. *Appl. Catal. B* **56**, 9–35 (2005).
10. Park, J., Nabae, Y., Hayakawa, T. & Kakimoto, M. A. Highly selective two-electron oxygen reduction catalyzed by mesoporous nitrogen-doped carbon. *ACS Catal.* **4**, 3749–3754 (2014).

© 2018 Macmillan Publishers Limited, part of Springer Nature. All rights reserved.

11. Jirkovsky, J. S. et al. Single atom hot-spots at Au–Pd nanoalloys for electrocatalytic H_2O_2 production. *J. Am. Chem. Soc.* **133**, 19432–19441 (2011).
12. Yang, S., Kim, J., Tak, Y. J., Soon, A. & Lee, H. Single-atom catalyst of platinum supported on titanium nitride for selective electrochemical reactions. *Angew. Chem. Int. Ed.* **55**, 2058–2062 (2016).
13. Zheng, Z., Ng, Y. H., Wang, D.-W. & Amal, R. Epitaxial growth of Au–Pt–Ni nanorods for direct high selectivity H_2O_2 production. *Adv. Mater.* **28**, 9949–9955 (2016).
14. Lee, Y.-H., Li, F., Chang, K.-H., Hu, C.-C. & Ohsak, T. Novel synthesis of N-doped porous carbons from collagen for electrocatalytic production of H_2O_2. *Appl. Catal. B Environ.* **126**, 208–214 (2012).
15. Paliteiro, C., Hamnett, A. & Goodenough, J. B. The electroreduction of oxygen on prolytic graphite. *J. Electroanal. Chem.* **233**, 147–159 (1987).
16. Tammeveski, K., Kontturi, K., Nichols, R. J., Potter, R. J. & Schiffrin, D. J. Surface redox catalysis for O_2 reduction on quinone-modified glassy carbon electrodes. *J. Electroanal. Chem.* **515**, 101–112 (2001).
17. Alvarez-Gallegos, A. & Pletcher, D. The removal of low level organics via hydrogen peroxide formed in a reticulated vitreous carbon cathode cell, Part 1. The electrosynthesis of hydrogen peroxide in aqueous acidic solutions. *Electrochim. Acta* **44**, 853–861 (1998).
18. Sarapuu, A., Vaik, K., Schiffrin, D. J. & Tammeveski, K. Electrochemical reduction of oxygen on anthraquinone-modified glassy carbon electrodes in alkaline solution. *J. Electroanal. Chem.* **541**, 23–29 (2003).
19. Yang, H. H. & McCreery, R. L. Elucidation of the mechanism of dioxygen reduction on metal-free carbon electrodes. *J. Electrochem. Soc.* **147**, 3420–3428 (2000).
20. Xu, J., Huang, W. H. & McCreery, R. L. Isotope and surface preparation effects on alkaline dioxygen reduction at carbon electrodes. *J. Electroanal. Chem.* **410**, 235–242 (1996).
21. Hasche, F., Oezaslan, M., Strasser, P. & Fellinger, T.-P. Electrocatalytic hydrogen peroxide formation on mesoporous non-metal nitrogen-doped carbon catalyst. *J. Energy Chem.* **25**, 251–257 (2016).
22. Tao, L. et al. Edge-rich and dopant-free graphene as a highly efficient metal-free electrocatalyst for the oxygen reduction reaction. *Chem. Commun.* **52**, 2764–2767 (2016).
23. Yan, D. et al. Defect chemistry of nonprecious-metal electrocatalysts for oxygen reactions. *Adv. Mater.* **29**, 1606459 (2017).
24. Cote, L. J., Kim, F. & Huang, J. Langmuir–Blodgett assembly of graphite oxide single layers. *J. Am. Chem. Soc.* **131**, 1043–1049 (2009).
25. Eda, G., Fanchini, G. & Chhowalla, M. Large-area ultrathin films of reduced graphene oxide as a transparent and flexible electronic material. *Nat. Nanotechnol.* **3**, 270–274 (2008).
26. Levich, B. The theory of concentration polarisation. *Discuss. Faraday Soc.* **1**, 37–49 (1947).
27. Zhou, R. F., Zheng, Y., Jaroniec, M. & Qiao, S. Z. Determination of the electron transfer number for the oxygen reduction reaction: from theory to experiment. *ACS Catal.* **6**, 4720–4728 (2016).
28. Bonakdarpour, A. et al. Impact of loading in RRDE experiments on Fe–N–C catalysts: two- or four-electron oxygen reduction? *Electron. Solid State Lett.* **11**, B105–B108 (2008).
29. Lerf, A., He, H., Forster, M. & Klinowski, J. Structure of graphite oxide revisited. *J. Phys. Chem. B* **102**, 4477–4482 (1998).
30. Acik, M. et al. Unusual infrared-absorption mechanism in thermally reduced graphene oxide. *Nat. Mater.* **9**, 840–845 (2010).
31. Acik, M. et al. The role of oxygen during thermal reduction of graphene oxide studied by infrared absorption spectroscopy. *J. Phys. Chem. C* **115**, 19761–19781 (2011).
32. Vijayarangamuthu, K. et al. Temporospatial control of graphene wettability. *Adv. Mater.* **28**, 661–667 (2016).
33. Bowling, R. J., Packard, R. T. & Mccreery, R. L. Activation of highly ordered pyrolytic-graphite for heterogeneous electron-transfer: relationship between electrochemical performance and carbon microstructure. *J. Am. Chem. Soc.* **111**, 1217–1223 (1989).
34. Wang, Y., Alsmeyer, D. C. & Mccreery, R. L. Raman-spectroscopy of carbon materials: structural basis of observed spectra. *Chem. Mater.* **2**, 557–563 (1990).
35. Shen, A. L. et al. Oxygen reduction reaction in a droplet on graphite: direct evidence that the edge is more active than the basal plane. *Angew. Chem. Int. Ed.* **53**, 10804–10808 (2014).
36. Schultz, B. J., Dennis, Lee, V. & Banerjee, S. An electron structure perspective of graphene interfaces. *RSC Adv.* **4**, 634–644 (2014).
37. Lee, V. et al. In situ near-edge X-ray absorption fine structure spectroscopy investigation of the thermal defunctionalization of graphene oxide. *J. Vac. Sci. Technol. B* **30**, 061206 (2012).
38. Kaniyoor, A. & Ramaprabhu, S. The Raman spectroscopic investigation of graphene oxide derived graphene. *AIP Adv.* **2**, 032183 (2012).
39. Diez-Betriu, X. et al. Raman spectroscopy for the study of reduction mechanisms and optimization of conductivity in graphene oxide thin films. *J. Mater. Chem. C* **1**, 6905–6912 (2013).
40. Ferrari, A. C. Raman spectroscopy of graphene and graphite: disorder, electron-phonon coupling, doping and nonadiabatic effects. *Solid State Commun.* **143**, 47–57 (2007).
41. Akhavan, O. The effect of heat treatment on formation of graphene thin films from graphene oxide nanosheets. *Carbon* **48**, 509–519 (2010).
42. Gao, Y. et al. Combustion synthesis of graphene oxide-TiO_2 hybrid materials for photodegradation of methyl orange. *Carbon* **50**, 4093–4101 (2012).
43. Lin, Y.-C., Lin, C.-Y. & Chiu, P.-W. Controllable graphene N-doping with ammonia plasma. *Appl. Phys. Lett.* **96**, 133110 (2010).
44. Newman, J. & Thomas-Alyea, K. E. Electrochemical Systems. (John Wiley & Sons, Hoboken, 2004).
45. McCloskey, B. D. et al. Combining accurate O_2 and Li_2O_2 assays to separate discharge and charge stability limitations in nonaqueous Li–O_2 batteries. *J. Phys. Chem. Lett.* **4**, 2989–2993 (2013).

Acknowledgements

B.D.M. and H.W.K. gratefully acknowledge support from the National Science Foundation under grant number CBET-1604927. H.W.K. also acknowledges support from the Basic Science Research Program through the National Research Foundation of Korea funded by the Ministry of Education (2016R1A6A3A03012382). N.K. gratefully acknowledges the Royal Society Newton International Fellowship. P.Y. acknowledges support from the Director of the Office of Science, Office of Basic Energy Sciences as part of the Chemical Sciences, Geosciences, and Biosciences Division of the US Department of Energy, under contract number DE-AC02-05CH11231 within the Catalysis Research Program (FWP number CH030201). The work at Molecular Foundry (XPS and scanning electron microscope) and Advanced Light Source (NEXAFS) was supported by the Office of Science, Office of Basic Energy Sciences of the US Department of Energy under contract number DE-AC02-05CH11231. H.W.K. gratefully acknowledges H. B. Park for guidance on graphene oxide synthesis, W. Kim for FTIR measurement and Y. Hwa for scanning electron microscope analysis. A. C. Luntz is also acknowledged for fruitful discussions on the potential mechanisms of ORR on mrGO materials.

Author contributions

H.W.K. contributed to the experimental planning, experimental measurements, data analysis and manuscript preparation. M.B.R. and N.K. performed the Raman spectroscopy, including in situ and ex situ measurements. L.Z. measured NEXAFS. J.G. and P.Y. provided experimental guidance for the NEXAFS and Raman measurements, respectively. B.D.M. contributed to the experimental planning, data analysis and manuscript preparation. All authors reviewed and commented on the manuscript before publication.

Competing interests

The authors declare no competing interests.

Additional information

Supplementary information is available for this paper at https://doi.org/10.1038/s41929-018-0044-2.

Reprints and permissions information is available at www.nature.com/reprints.

Correspondence and requests for materials should be addressed to B.D.M.

Publisher's note: Springer Nature remains neutral with regard to jurisdictional claims in published maps and institutional affiliations.

© 2018 Macmillan Publishers Limited, part of Springer Nature. All rights reserved.